Electronic Supplementary Information

# Defect-Engineering of Liquid-Phase Exfoliated 2D Semiconductors: Stepwise Covalent Growth of Electronic Lateral Hetero-Networks

Antonio Gaetano Ricciardulli,[a] Christopher E. Petoukhoff, [b] Anna Zhuravlova,[a] Adam G. Kelly,[c] Chun Ma,[a] Frédéric Laquai,[b] Jonathan N. Coleman,[c] and Paolo Samorì[a]*

[a] Université de Strasbourg, CNRS, ISIS UMR 7006, 8 allée Gaspard Monge, 67000 Strasbourg, France

[b] King Abdullah University of Science and Technology (KAUST), Physical Sciences and Engineering Division (PSE), KAUST Solar Center (KSC), Thuwal, 23955-6900, Kingdom of Saudi Arabia

[c] School of Physics, Centre for Research on Adaptive Nanostructures and Nanodevices (CRANN) and Advanced Materials and Bioengineering Research (AMBER), Trinity College Dublin, Dublin 2, Ireland

*Corresponding author: samori@unistra.fr

**Table of Contents**


| | page |
|---|---|
| 1. Experimental Methods | S3 |
| 2. Controlled experiments on conventional deposition techniques | S7 |
| 3. Optical and morphological investigation | S8 |
| 4. X-ray photoelectron spectroscopy (XPS) analysis | S14 |
| 5. Raman spectroscopy analysis | S17 |
| 6. Electrochemical impedance spectroscopy (EIS) | S21 |
| 7. Transient absorption (TA) spectroscopy analysis | S25 |
| 8. Electrical characteristics in FET based on $MoS_2$-$WS_2$ heterostructure | S33 |
| 9. Field-effect mobility comparison | S35 |
| References | S37 |

## 1. Experimental Methods

*Production of liquid-phase exfoliated $MoS_2$ and $WS_2$ inks.* $MoS_2$ and $WS_2$ inks are obtained by sonicating pristine powders (Sigma Aldrich, purity > 99%) in *N*-Methyl-2-pyrrolidone (NMP) according to a previously reported procedure.[1] The dispersions with initial concentration of 20 mg $ml^{-1}$ in NMP were sonicated for 1 hour using a horn tip sonicator (Sonics Vibra-cell VCX-750 ultrasonic processor) at 60% amplitude and subsequently centrifuged at 3218 g for 1 hour using a Hettich Mickro 220R. The supernatant was discarded to remove potential contaminants from the starting powder. Then, the sediment was redispersed in fresh NMP and sonicated under the same conditions for 5 hours. As a result, polydisperse stock dispersions were yielded, from which flakes can be size selected by stepwise centrifugation. In short, to remove the largest aggregates, the polydisperse stocks are first centrifuged at 106.4 g for 90 min, and the sediment retained for future exfoliation. The supernatant is further centrifuged at 425 g for 90 min to separate the smaller flakes. This sediment is finally redispersed in isopropanol (IPA).

*Film formation via microfluidic approach.* $Si/SiO_2$ substrates (15 × 15 $mm^2$) were rinsed with acetone and 2-propanol to remove any potential contaminant and their surface activated by UV/ozone treatment (NovaScan, Digital UV/Ozone System) for 20 min. Afterwards, to enhance the wettability, the substrates were immersed in 1% 3-(aminopropyl)triethoxysilane (APTES, Alfa Aesar, 98%) solution in water for 30 mins. Then, 0.5 mg $mL^{-1}$ dispersions of $MoS_2$ and $WS_2$ in IPA were prepared separately and sonicated for 30 mins in an ice bath. To fabricate the films, a peristaltic pump (Heidolph Hei-Flow Precision 01) was used and IPA dispersions of $MoS_2$ and $WS_2$ were alternated. Between each deposition step, a 50 mM solution of 1,4-benzenedithiol (BDT, Sigma Aldrich, ≥ 99%) was circulated. Further details on the film formation are provided in the following SI section, in the text related to Figure S1.

*Electrodes fabrication for spectroscopical study.* The films were grown on prepatterned substrates to carry out impedance spectroscopy analysis. The electrodes were patterned on a *n*-doped standard $Si/SiO_2$ (oxide thickness: 90 nm thickness, size: 15 × 15 mm) by maskless photolithography (Microtech LW405B laser writer) using AZ1505 photoresist and MIF726 developer. The channel

length and width were both 10 $\mu$m. Then, 3 nm chromium and 40 nm gold were thermally evaporated in turn with high vacuum Plassys MEB 300 followed by sonication-assisted lift-off in acetone. An Olympus BX51 optical microscope was employed to monitor the quality of the lift-off.

*Atomic force microscopy (AFM).* AFM investigation was performed using a Bruker Dimension Icon operating in air by tapping mode (TESPA-V2 tip, k = 42 N $m^{-1}$).

*Scanning electron microscopy (SEM).* SEM images were captured using a FEI Quanta 250 FEG scanning electron microscope operated in high vacuum mode ($10^{-4}$ Pa) and with accelerating voltages of 30 kV for the incident beam.

*X-ray photoelectron spectroscopy (XPS).* XPS analysis was carried out with a Thermo Scientific K-Alpha X-ray photoelectron spectrometer, equipped with a chamber pressure of ~$10^{-9}$ mbar and an Al anode X-ray source (1486 eV radiation). Spot sizes of 400 $\mu$m and pass energies of 200.00 eV for wide energy scans and 20.00 eV for high-resolution scans were used on fabricated films based both on pristine materials and lateral heterostructures, respectively. The peak fitting of high-resolution XPS spectra S2p, Mo3d and W4f regions was performed using characteristic doublets with the following fitting constraints: i) S2p, L/G Mix = 30%, spin-orbit splitting = 1.20 ± 0.1 eV and intensity ratio = 0.511 for S2p3/2 and S2p 1/2 components; ii) Mo3d, L/G Mix = 30%, spin-orbit splitting = 3.15 (+0.2-0.1) eV and intensity ratio = 0.690 for Mo3d5/2 and Mo3d3/2 components; iii) W4f, L/G Mix = 30%, spin-orbit splitting = 2.15 ± (+0.2-0.1) eV and intensity ratio = 0.788 for W4f7/2 and W4f5/2 components. For quantification, corresponding atomic scattering factors were extracted from quantification library of the Avantage software package and automatically corrected for the instrument transmission function.

*Raman spectroscopy.* Raman spectroscopy measurements were performed with a Renishaw inVia spectrometer at 532 nm, which is equipped with a 2D-CCD camera. To avoid sample damages, the films were irradiated with laser power ≤ 1% and exposure times ≤ 10 s.

*Electrochemical impedance spectroscopy (EIS).* EIS measurements in NaCl aqueous solution, used as electrolyte, were carried out operating a Metrohm Autolab PGSTAT204 potentiostat coupled with a mini probe station (Everbeing Int'l Corp.). EIS tests were performed from high to low frequencies, using a frequency range of 0.1 - $10^5$ Hz and a sine-wave voltage signal amplitude of 50 mV (root-mean-square, RMS). Data was analyzed with the software NOVA, Metrohm Autolab.

*Electrical characterizations.* The field-effect transistors (FETs) performance characteristics were measured by a software-controlled source meter (Keithley 2636A) at room temperature and under nitrogen atmosphere into a glovebox. A platinum wire and a droplet of 1-ethyl-3-methylimidazolium bis(trifluoromethylsulfonyl)imide (EMI-TFSI), purchased from TCI Chemicals, were used as the gate electrode and the ionic liquid gate dielectric, respectively. Thin films for electrical characterizations were built bottom-contact *n*-doped $Si/SiO_2$ substrates (15 × 15 mm; Fraunhofer IPMS), consisting of thermally grown $SiO_2$ (230 nm thick) with interdigitated gold electrodes spaced at 2.5 $\mu$m and channel length of 10 mm.

*Transient absorption (TA) spectroscopy.* TA spectroscopy was carried out using a home-built pump-probe setup. The output of a Ti:sapphire amplifier (Coherent LEGEND DUO, 800 nm, 4.5 mJ, 3 kHz, 100 fs) was split into four beams (2 mJ, 1 mJ, 1 mJ, and 0.5 mJ). Three of them were used to separately pump three optical parametric amplifiers (OPA; Light Conversion TOPAS Prime). One of the 1 mJ TOPAS was used to generate wavelength-tunable pump pulses (240-2600 nm, using Light Conversion NIRUVIS extension), which was fixed at 500 nm with a fluence of 9.5 μJ/$cm^2$. The second 1 mJ TOPAS was used to generate signal and idler only (1160-2600 nm), which was fixed to 1300 nm and was used as the seed for white light generation by focusing a portion of it through a continuously moving $CaF_2$ crystal, thereby generating a white light

supercontinuum from 350 nm to 1100 nm. The pump-probe delay time was achieved by varying the probe path length using a broadband retroreflector mounted on a 600 mm automated mechanical delay stage (Thorlabs optical delay line ODL600/M), generating delays from -400 ps to 7 ns.

Pump and probe beams were focused on the sample to spot sizes of 0.704 mm and 0.049 mm average diameter (from a Gaussian fit at 86.5% intensity), as measured using a beam profiler (Coherent LaserCam-HR II). The samples were kept under a dynamic vacuum of $<10^{-5}$ mbar, and pump and probe beams were incident on the film-side of the sample. The transmitted fraction of the white light was guided to a custom-made prism spectrograph (Entwicklungsbüro Stresing) where it was dispersed by a prism onto a 512-pixel NMOS linear image sensor (Hamamatsu S8381-512Q). The probe pulse repetition rate was 3 kHz, while the excitation pulses were mechanically chopped to 1.5 kHz, and the detector array was read out at 3 kHz. Adjacent diode readings corresponding to the transmission of the sample after excitation and in the absence of an excitation pulse were used to calculate ΔT/T. Measurements were averaged over several thousand shots to obtain a good signal-to-noise ratio. The chirp induced by the transmissive optics was corrected with a home-built Matlab code.

To account for the spectral shifts of the excited state signals, TA spectra were fit with a sum of either 1, 2, or 3 Gaussians at every pump-probe delay time to determine the peak shifts (**Figure S22**). Kinetic traces of each exciton feature were obtained by taking the maximum ΔT/T value at the wavelength determined from the Gaussian fit for each species to account for the spectral shifts. (**Figure S23**). The kinetics were fitted with a biexponential decay equation: $\Delta T/T = A_0 + A_1 e^{\left(\left(-t/\tau_1\right)\right)} + A_2 e^{\left(\left(-t/\tau_2\right)\right)}$, where $t$ is the pump-probe delay time, $A_i$ are the amplitudes of the decay components, and $t_i$ are the lifetimes of the decay components, and the average lifetimes ($t_{ave}$) were calculated by taking the amplitude-average of the fast and slow components.

## 2. Controlled experiments on conventional deposition techniques

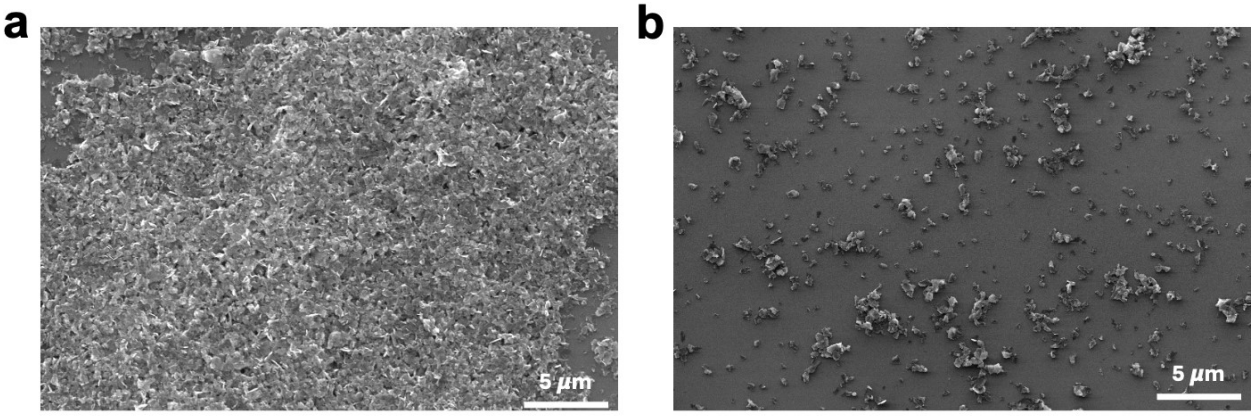


**Figure S1.** SEM images on deposition of LPE TMDs flakes through (a) drop-casting and (b) spin-coating. As a result of the lack of assembly control, the deposited films display aggregated flakes and uneven coverage, hindering the use of alternating flakes to build lateral hetero-networks.

## 3. Optical, morphological and topographical investigation

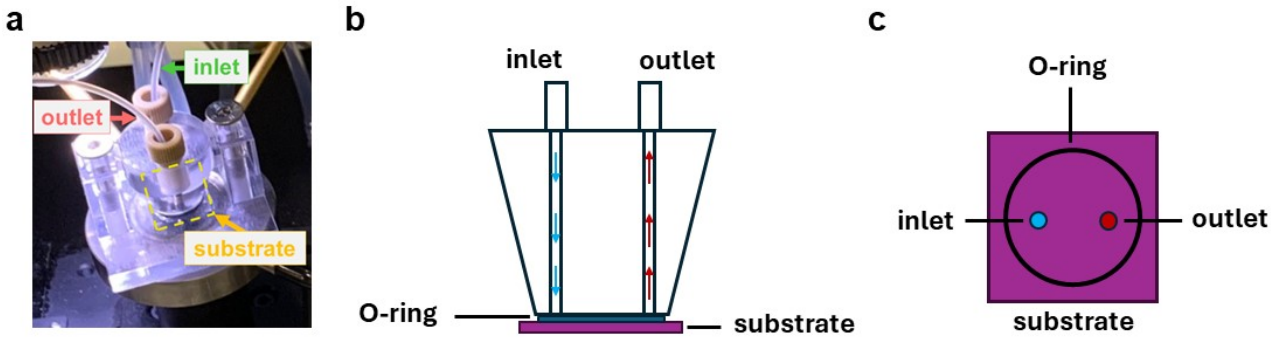


**Figure S2.** (a) Optical image of the microfluidic chamber; schematic illustration of the microfluidic setup: (b) side- and (c) top-view.

The films were growth stepwise using a microfluidic setup including a microfluidic chamber (Figure S1) with an internal volume of ~12 $\mu$L and a peristaltic pump. The optimal flow rate of 0.6 mL $min^{-1}$ was kept constant throughout the deposition. Moreover, a tube diameter of 0.8 mm was employed to avoid aggregation of flakes during the fabrication process, which can lead to clogging, and thus to uneven coatings. First, the substrate was placed in the chamber and coated with $MoS_2$ by flowing the dispersion of $MoS_2$ in IPA for 3 minutes. This step yielded randomly distributed $MoS_2$ flakes on the surface (Figure S3). In contrast, exposure times lower or higher than 3 minutes led to scarce or dense $MoS_2$ distribution, respectively. Then, a 50 mM solution of BDT in IPA was circulated into the system for 2 minutes to trigger the functionalization at the $MoS_2$ defect sites. Afterwards, a dispersion of $WS_2$ in IPA was used for 10 minutes to enable the linking with free thiols terminals, granting linking through defects and formation of a first $MoS_2$-BDT-$WS_2$ in-plane network. Subsequently, BDT was used as described before and the previous steps repeated to yield a lateral heterostructure. It worth noting that between each step, the whole system was flushed with IPA to clean the tubes and chamber by a possible excess of material and remove any TMD flake or BDT molecules that did not attach onto the surface of the substrate or where covalently tethered to the forming network. An overview of further processing parameters that have been controlled, such as flow rate, tube diameter, dispersions concentration, is provided in Figure S4.

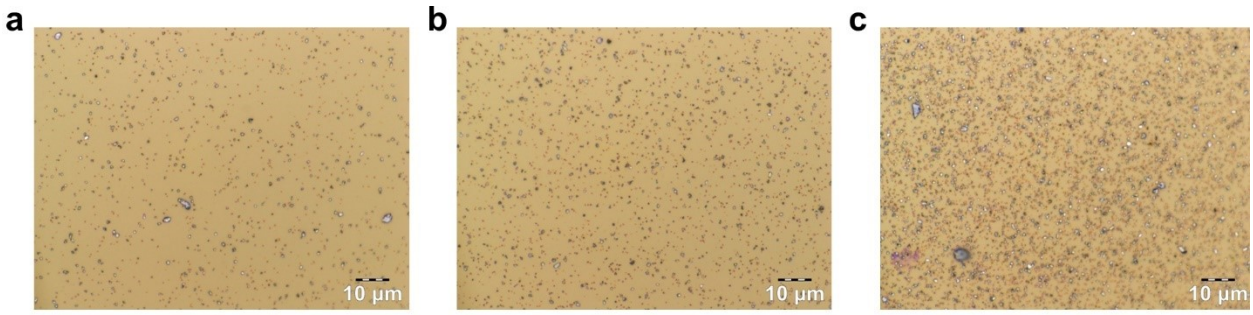


**Figure S3.** Optical images of $Si/SiO_2$ substrate coated with $MoS_2$ after (a) 2, (b) 3 and (c) 5 minutes of $MoS_2$ dispersion flow.

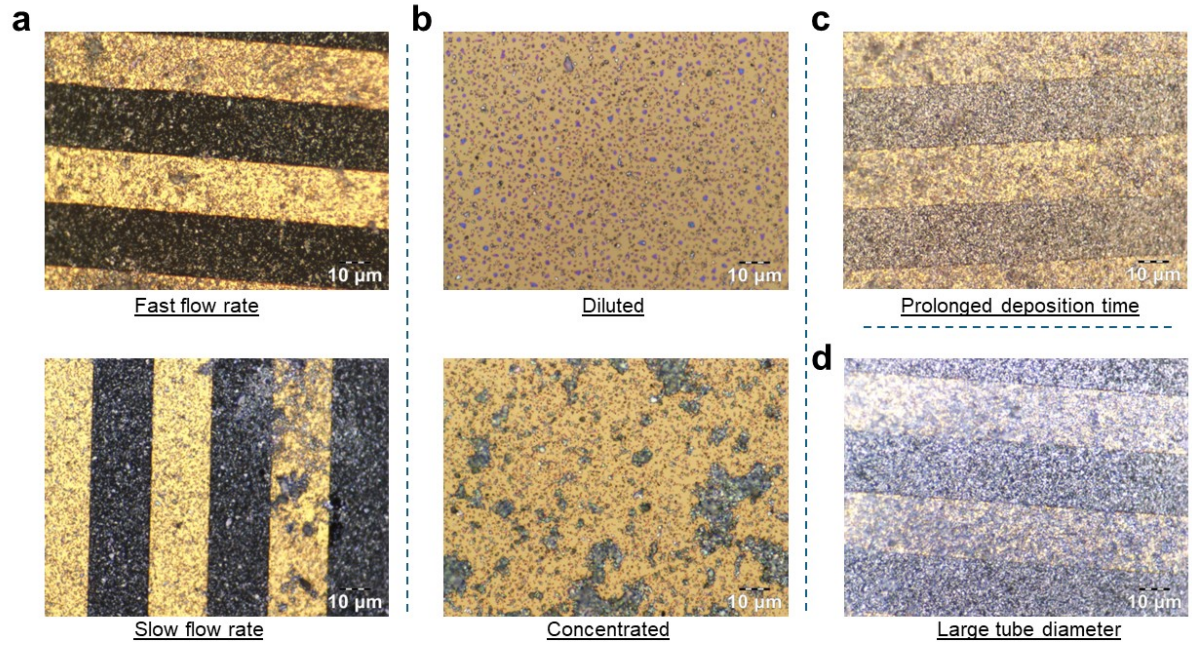


**Figure S4.** Processing parameters control. (a) Flow rates diverging from the optimal value of 0.6 mL $min^{-1}$ led to uneven coatings, as observed by using rates of 1.0 mL $min^{-1}$ (top) and 0.2 mL $min^{-1}$ (bottom), respectively. (b) Concentrations of as-synthesized $MoS_2$ and $WS_2$ inks, above 1 mg $mL^{-}1$ led to the formation of aggregated clusters of TMDs and inhomogeneous coatings (bottom). In contrast, the diluted counterparts (0.1 mg $mL^{-1}$) yielded scarce coverage (top). The optimal dispersion concentration in the microfluidic approach is 0.5 mg $mL^{-1}$. The use of longer deposition times (c) or (d) large tube diameter (d), such as 1.2 mm, produced irregular and rough films.

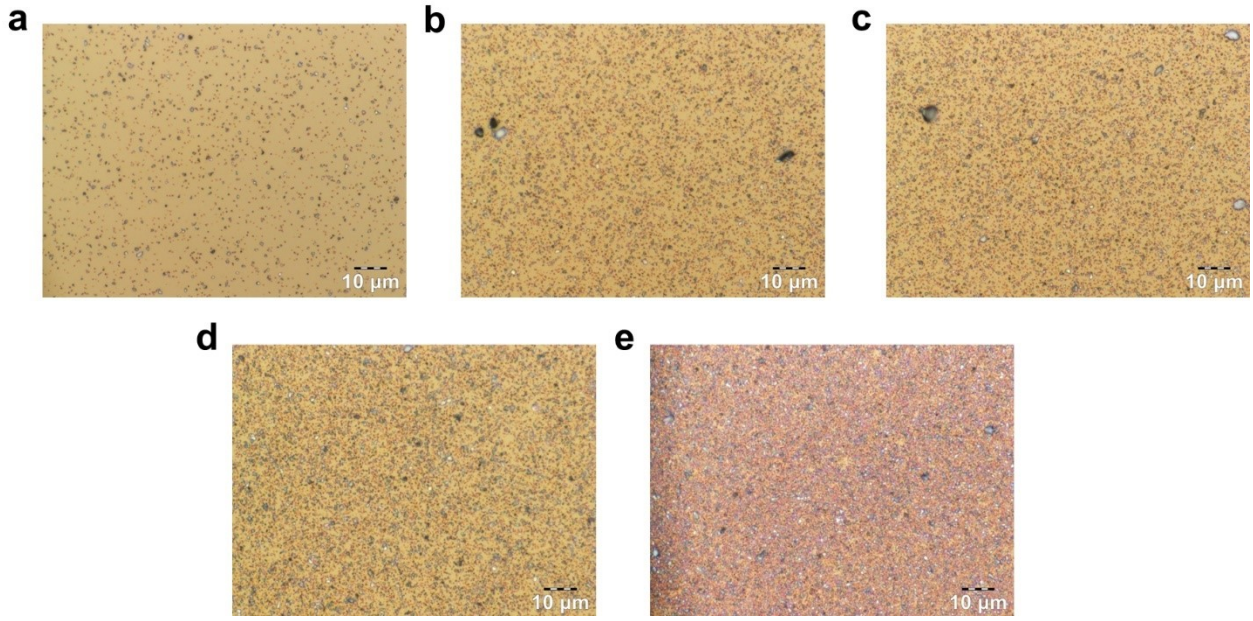


**Figure S5.** Optical microscopy survey images of the in-plane growth of the $MoS_2$-$WS_2$ heterostructure assisted by BDT bridging. Corresponding film after the stepwise deposition of (a) $MoS_2$, (b) $WS_2$, (c) $MoS_2$, (d) $WS_2$ and (e) $MoS_2$. BDT solution in IPA was circulating after between steps.

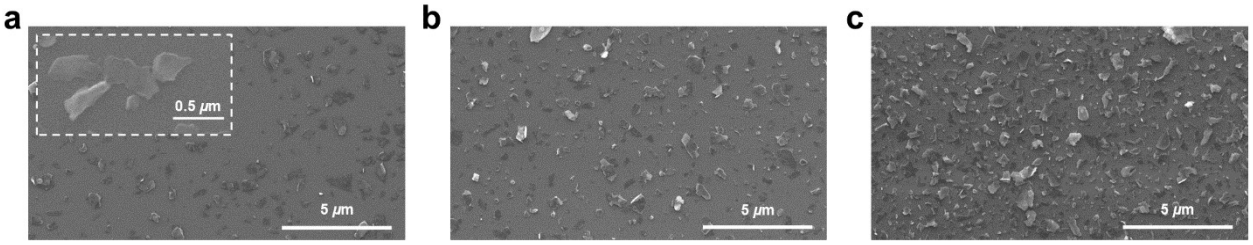


**Figure S6.** SEM images of the intermediate steps of the lateral heterostructure corresponding to (a) $Mo_2$-$WS_2$ (inset: in-plane junction within flakes), (b) $MoS_2$-$WS_2$-$MoS_2$ and (c) $MoS_2$-$WS_2$-$MoS_2$-$WS_2$.

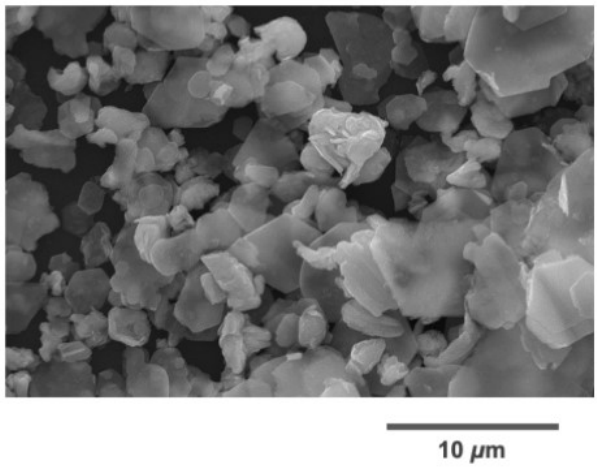


**Figure S7.** SEM image of a film based on $MoS_2$-$WS_2$ hetero-network after further deposition steps exceeding the optimization threshold, which result in undesirable aggregations and vertical stacking of flakes.

## 4. X-ray photoelectron spectroscopy (XPS) analysis

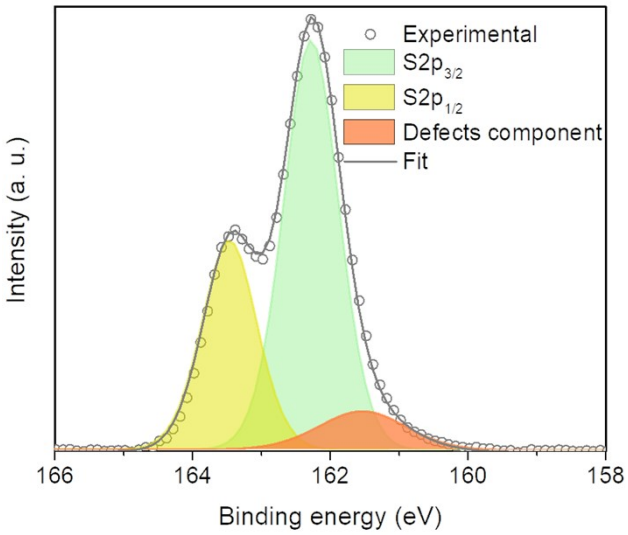


**Figure S8.** High-resolution (HR) XPS spectrum of the S 2p region in pristine $MoS_2$-$WS_2$ blend.

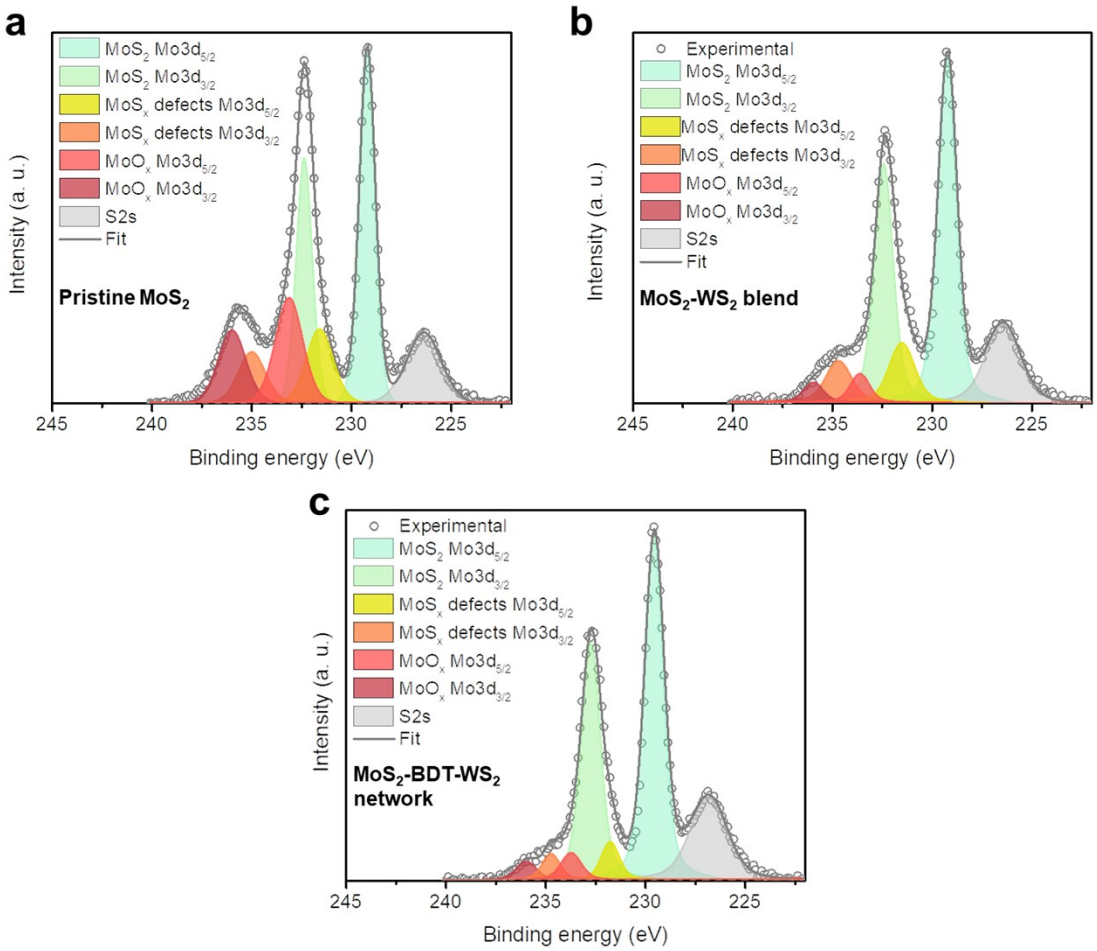


**Figure S9.** HR-XPS spectra of Mo 3d peak in (a) pristine $MoS_2$, (b) $MoS_2$-$WS_2$ blend and (c) $MoS_2$-$WS_2$ BDT-linked lateral heterostructure.

The Mo 3d region of $MoS_2$, pristine $MoS_2$-$WS_2$ blend and $MoS_2$-BDT-$WS_2$ lateral heterostructure is characterized by a set of doublets emerging from the Mo $3d_{5/2}$ and Mo $3d_{3/2}$ spin-orbital splitting (Figure S9). The intense characteristic $MoS_2$ doublet appears at ~229.3 and ~232.5 eV. In contrast, the peaks at ~233.4 and ~236 eV correspond to oxidized Mo species. Moreover, the defect component can be deconvoluted at ~231.5 and ~234.7 eV. The S2s singlet is displayed at ~226.6 eV. The significant decrease of the relative area of the defect component from 16% in pristine $MoS_2$ and 15% in the pristine $MoS_2$-$WS_2$ blend to 8.6% in the $MoS_2$-BDT-$WS_2$ network suggests the successful functionalization by BDT through sulfur vacancies healing.[2] These results further support the evidence of the healing process confirmed by the HR-XPS analysis of S 2p region.

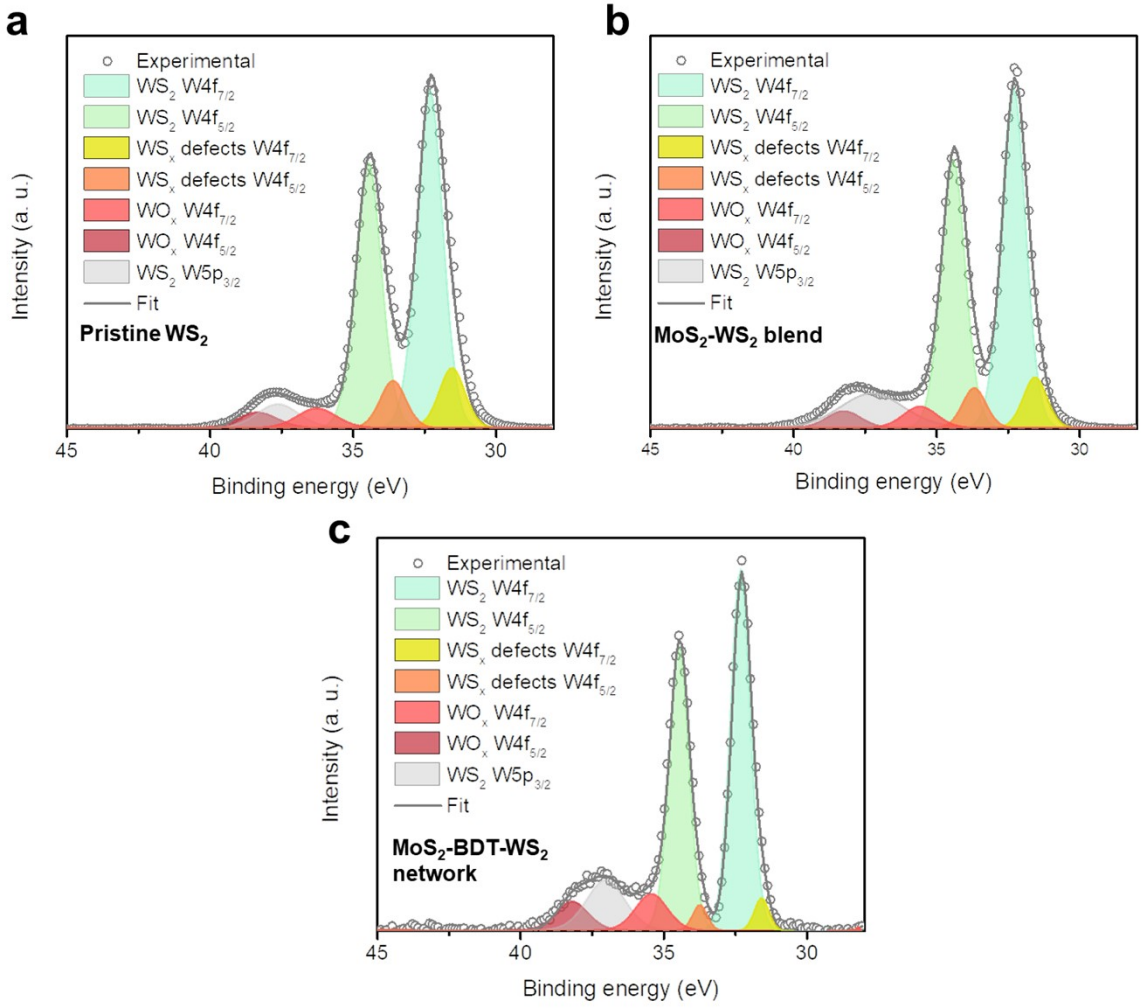


**Figure S10.** HR-XPS spectra of W 4f peak in (a) pristine $WS_2$, (b) $MoS_2$-$WS_2$ blend and (c) $MoS_2$-$WS_2$ BDT-linked lateral heterostructure.

The W 4f region features a set of doublets due to the W $4f_{7/2}$ and W $4f_{5/2}$ spin-orbital splitting (Figure S9). The intense $WS_2$ peaks lay at ~32.3 and ~34.5 eV. The oxidized tungsten impurity is present at ~36 and ~38.3 eV. The defect component of $WS_2$ emerges at ~31.5 and ~33.7 eV. In addition, this energy region is characterized by a W $5p_{3/2}$ peak at ~37.2 eV. As for $MoS_2$ (Figure S10), the relative area of the defect component in $WS_2$ decreases from 18% for pristine $WS_2$ and 15% for the $MoS_2$-$WS_2$ blend to 7% in the $MoS_2$-BDT-$WS_2$ film. These results further prove the successful healing of defects in $WS_2$ through BDT functionalization,[3] as also supported by the reduction of the defect density displayed in the S 2p region.

**5. Raman spectroscopy analysis**

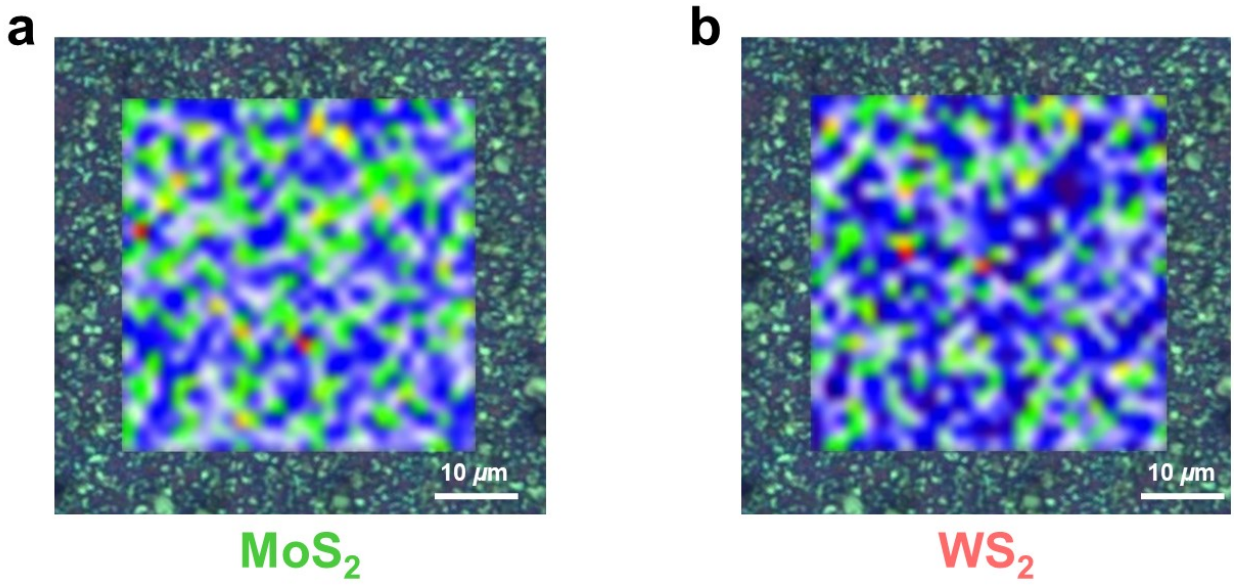


**Figure S11.** Raman mapping of (a) $MoS_2$ and (b) $WS_2$ building units in the BDT-linked heterostructure.

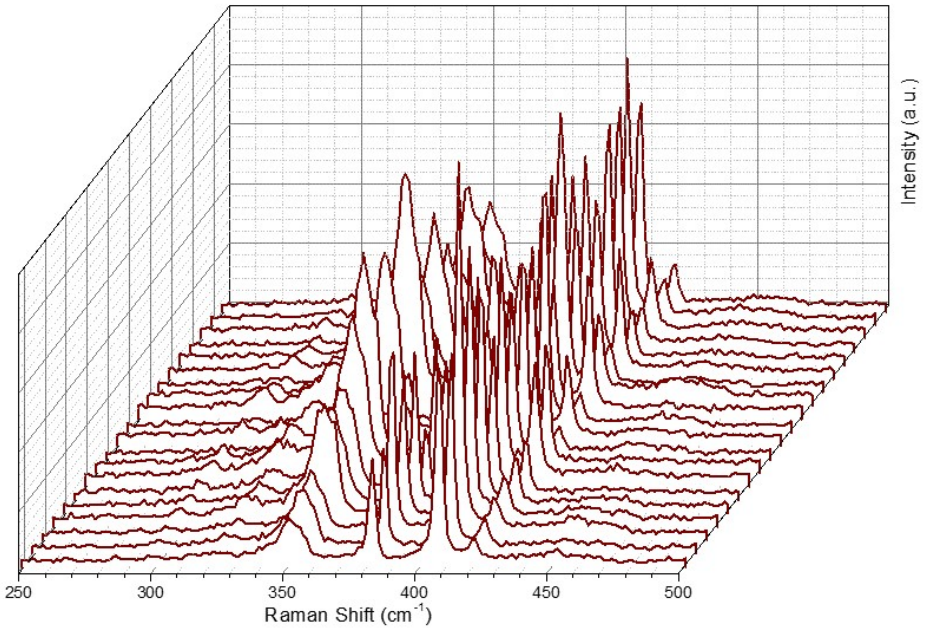


**Figure S12.** Random selected Raman spectra of the $MoS_2$-BDT-$WS_2$ hetero-network showing the characteristic bands of both $MoS_2$ and $WS_2$, revealing equal distribution of the 2D building units. Furthermore, the characteristic Raman features of $MoS_2$ and $WS_2$ are retained, indicating that the BDT does not induce any apparent change to the intrinsic structural features of the TMDs.

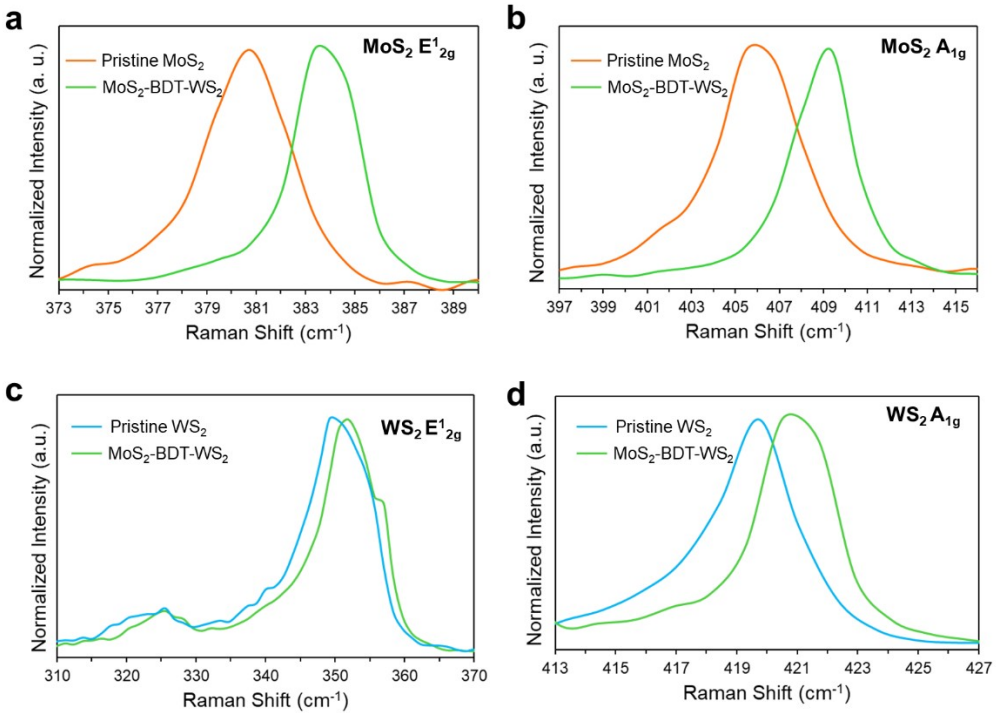


**Figure S13.** Comparison of (a) $E^1_{2g}$ and (b) $A_{1g}$ Raman peaks of $MoS_2$ in pristine LPE $MoS_2$ film and $MoS_2$-BDT-$WS_2$ lateral heterostructure. (c) $E^1_{2g}$ and (d) $A_{1g}$ Raman peaks of $WS_2$ in pristine LPE $WS_2$ film and $MoS_2$-BDT-$WS_2$ heterostructure.

A significant blue shift is observed for $E^1_{2g}$ and $A_{1g}$ peaks, related to in-plane and out-of-plane vibrations, respectively, for both $MoS_2$ and $WS_2$ in the $MoS_2$-BDT-$WS_2$ film (Figure S13). Such variations are in agreement with the suppression of defects-activated modes upon BDT healing.[4] As the coverage of the $MoS_2$-BDT-$WS_2$ heterostructure is larger than the one of both pristine films and simple blend, the flake-substrate interaction at the interface is critical. Thus, the out-of-plane mode tends inevitably to be stabilized as the nanosheets approach the surface of the substrate, leading to a significant blue shift in both the $A_{1g}$ components of $MoS_2$ and $WS_2$. Additionally, cross-linking with BDT plays a significant role in the system rigidity, further constraining the out-of-plane mode. Moreover, the frequency of the $E^1_{2g}$ mode is strictly correlated with defect density. Hence, a blue shift of the vibrational frequencies occurs upon decrease of defect density.[4] Further evidence is provided by the FHWM contraction that occurs for the $E^1_{2g}$ and $A_{1g}$ features of both $MoS_2$ and $WS_2$ in the heterostructure built by employing BDT as linker (Table S1).

| **Material** | **FWHM $E^1_{2g}$ ($cm^{-1}$)** | **FWHM $A1_g$ ($cm^{-1}$)** |
|---|---|---|
| $MoS_2$ | 4.20 ± 0.25 | 4.36 ± 0.25 |
| $MoS_2$ ($MoS_2$-BDT-$WS_2$) | 2.82 ± 0.48 | 3.45 ± 0.49 |
| $WS_2$ | 11.39 ± 0.37 | 3.35 ± 0.15 |
| $WS_2$ ($MoS_2$-BDT-$WS_2$) | 10.63 ± 0.24 | 3.01 ± 0.23 |

**Table S1.** Statistical analysis over 20 Raman spectra of FWHM of $E^1_{2g}$ and $A_{1g}$ peaks of pristine $MoS_2$, pristine LPE $WS_2$ and $MoS_2$-BDT-$WS_2$ films.

## 6. Electrochemical impedance spectroscopy (EIS)

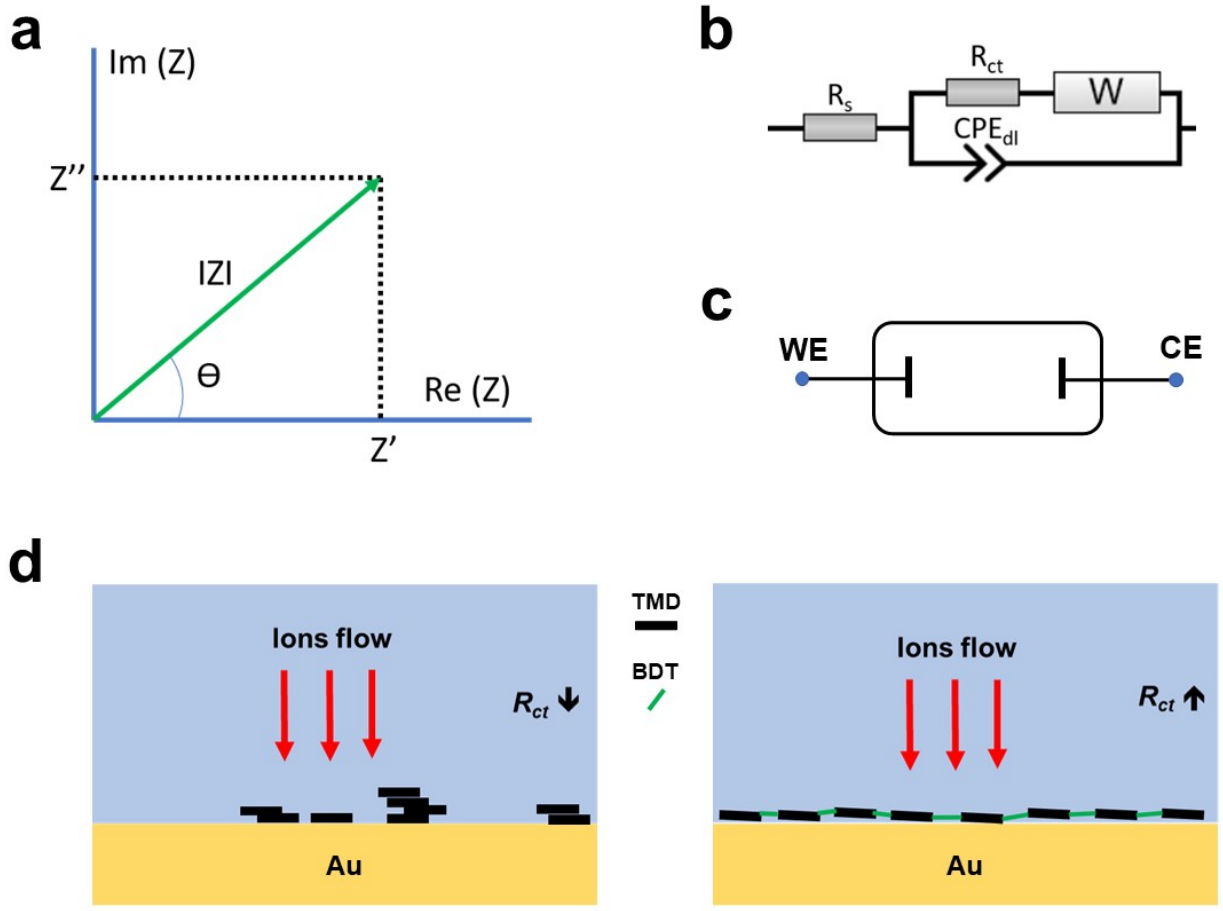


**Figure S14.** (a) Schematic representation of the impedance $Z$. $Z^{'}$ and $Z^{''}$ are real and imaginary components of $Z$, θ is the phase and $|Z|$ is the modulus. (b) Schematic illustration of the Randle's circuit that is used in this study. (c) Scheme of the symmetrical two-electrode setup. (d) Schematic illustration of ionic charge transfer process for pristine LPE TMD-based film (left) and TMD lateral heterostructure.

EIS is a powerful tool for the study of thin films and interfaces. EIS relies on the small amplitude sinusoidal potential or current perturbations at different frequencies.[5,6] Accordingly, the sinusoidal response of current or potential is collected and translated to the electrochemical impedance of the cell at a given frequency:

$$Z(\omega) = \frac{\tilde{V}(\omega)}{\tilde{I}(\omega)} \quad (1)$$

$$Z(\omega) = \left|\frac{\tilde{V}(\omega)}{\tilde{I}(\omega)}\right|(cos\varphi(\omega) + isin\varphi(\omega)) = Z^{'} + iZ^{''} \quad (2)$$

$$|Z| = \sqrt{(Z^{'})^2 + (iZ^{''})^2} \quad (3)$$

where $\omega$ is the angular frequency and can be expressed through the frequency $f$ as $\omega = 2\pi f$, $\varphi$ is the phase angle between the input and the response signals, $\tilde{V}$ and $\tilde{I}$ are phasors of the corresponding sinusoidal functions. The overall impedance $Z$ is frequency-dependent and can be expressed as a sum of its real ($Z^{'}$) and imaginary ($Z^{''}$) parts (1,2),[6] while the modulus of the impedance is calculated as the square root of the squared $Z^{'}$ and $Z^{''}$ (3).[7] The graphical representation of the impedance and its components is given in Figure S11a. Typically, EIS results are represented in the form of Nyquist plots where the *x* and *y* axes are $Z^{'}$ and $Z^{''}$, respectively. These diagrams allow the graphical separation of the processes that occur in the electrochemical cell. Ultimately, every system can be modelled with an equivalent circuit composed of primitive circuit elements. Each element is associated with a real process in the cell. The Randle's equivalent circuit, which comprises solution resistance $R_s$, charge transfer resistance $R_{ct}$, double layer capacitance $CPE_{dl}$ and diffusion-related Warburg impedance $W$, was employed in this study (Figure S11b). Such model provides direct comparison among all the dataset with minimized error.

The experimental setup (Figure S12c) consists of a symmetrical two-electrode system that is composed of the identical interdigitated working electrode (WE) and counter electrode (CE), a TMD film that grown stepwise on top of WE and CE, and aqueous electrolyte. Thus, the measured impedance includes all the contributions of the processes between WE and CE.[6] In such system, the ions migrate from the electrolyte towards the electrodes upon the perturbation of the potential, generating ion conductance. The TMD film, formed between the electrodes and the electrolyte, acts as a barrier to the ion flow, hindering the charge transfer at the interface. Therefore, the lateral and uniform growth of the film leads to a considerable $R_{ct}$ increase (Figure S11d).

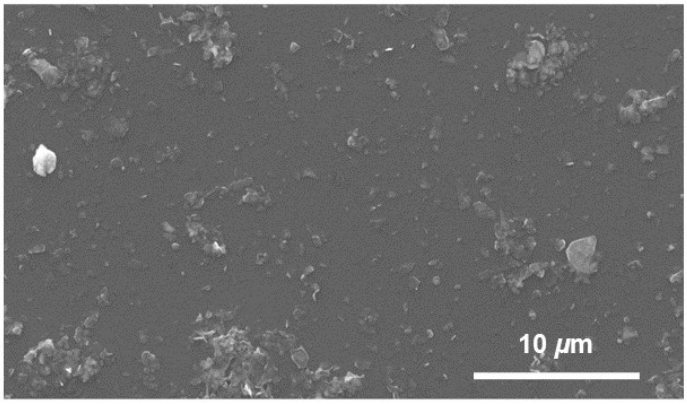


**Figure S15.** SEM image of a film fabricated by alternating $MoS_2$ and $WS_2$ multiple times without using BDT as intermediate step.

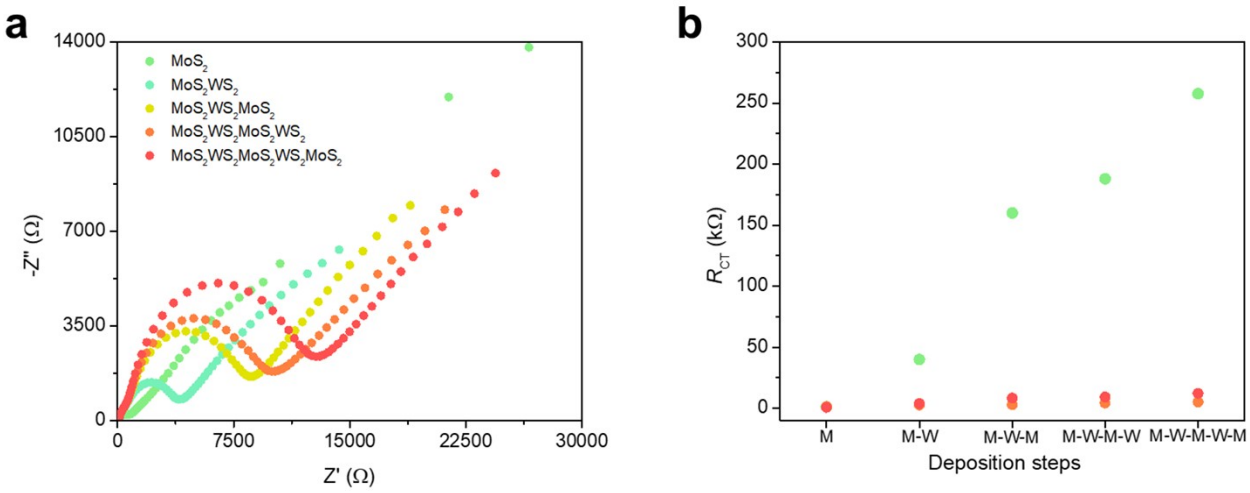


**Figure S16.** (a) EIS signal evolution upon increase of $MoS_2$ and $WS_2$ deposition. Between each step, an IPA solution of thiophenol is circulated. (b) $R_{ct}$ increase after each $MoS_2$ and $WS_2$ deposition step in films with BDT (green), thiophenol (red) and without any molecular linker (orange).

## 7. Transient spectroscopy (TA) analysis

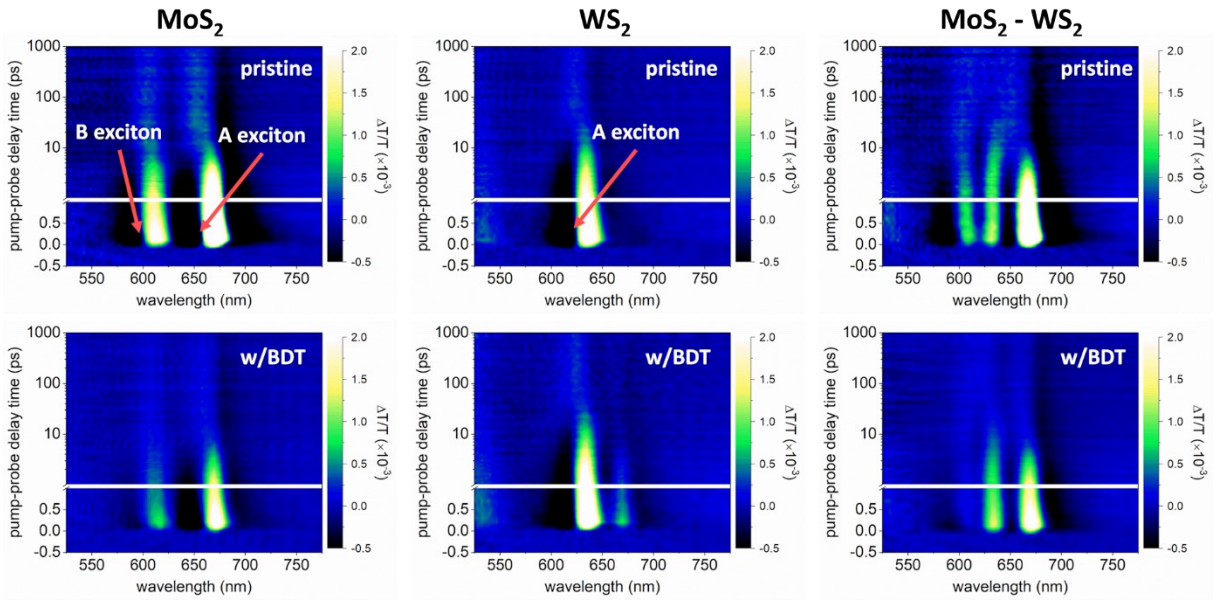


**Figure S17**. Contour plots of transient absorption (TA) spectra of the pristine $MoS_2$, $WS_2$, and $MoS_2$-$WS_2$ heterostructures (top row), and the samples treated with BDT (bottom row).

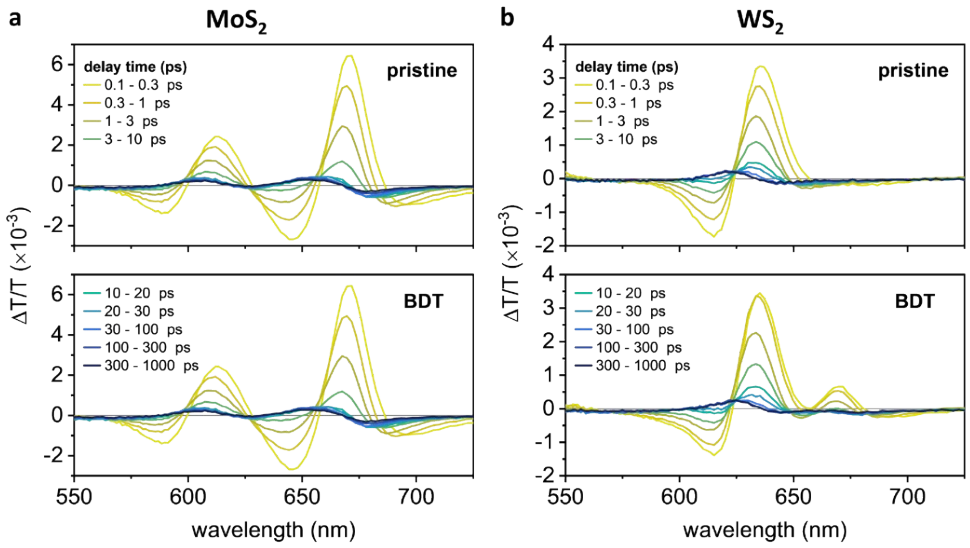


**Figure S18**. Transient absorption (TA) spectra of the isolated TMDs with and without BDT: (a) $MoS_2$ and (b) $WS_2$. The spectra are averaged over the pump-probe delay times listed in the legend.

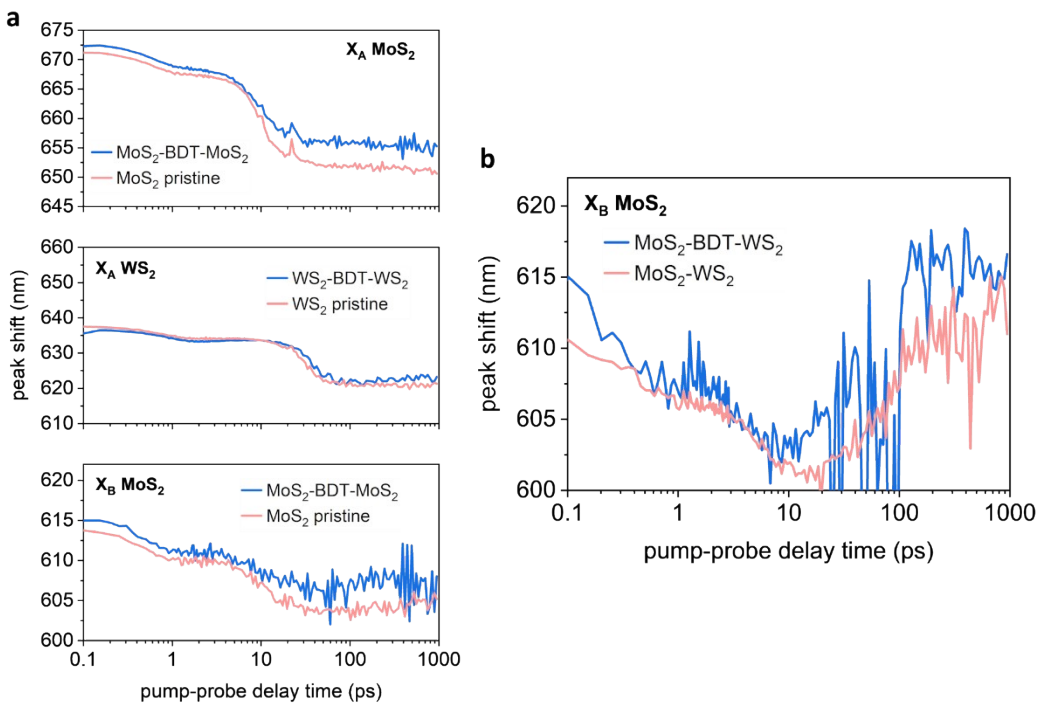


**Figure S19**. Peak shifts for the reported species, with or without BDT, as determined from Gaussian fits to the individual peaks, for: (a) isolated TMDs: $X_A$ of $MoS_2$ (top); $X_A$ of $WS_2$ (middle); $X_B$ of $MoS_2$ (bottom); or (b) $X_B$ of $MoS_2$ in the $MoS_2$-$WS_2$ heterostructures.

All the photoexcited species within the neat TMD materials, with or without BDT, blue-shifted with increasing pump-probe delay time, due to their bandgaps returning to their ground-state values (**Figure S19a**). $X_B$ of $MoS_2$ in the heterostructures, however, exhibited different behavior from the pristine materials (**Figure S19b**). The peaks blue-shifted up to ~10-20 ps, at which point they again red-shifted. We attribute this to competition between relaxation of the bandgap renormalization at faster timescales with the slow transfer of trapped carriers at longer timescales.[8]

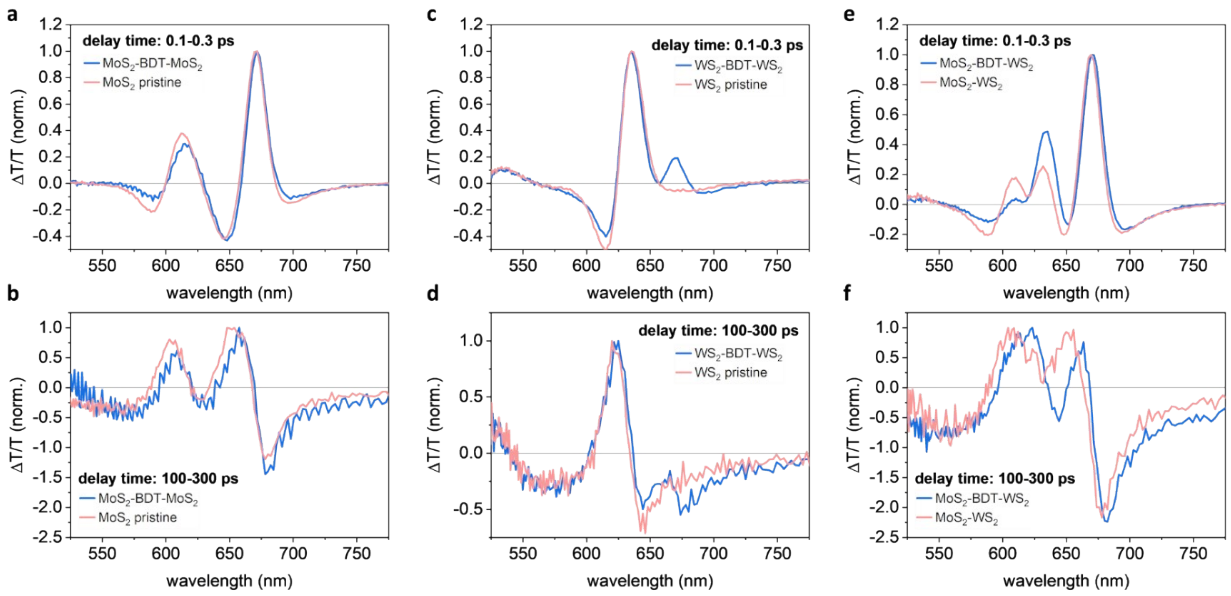


**Figure S20**. Transient absorption (TA) spectra of $MoS_2$ (a,b), $WS_2$ (c,d), and $MoS_2$-$WS_2$ heterostructures (e,f) with and without BDT. The spectra are averaged over early delay times (a,c,e: 0.1-0.3 ps) or late delay times (b,d,f: 100-300 ps).

We note that $X_A$ and $X_B$ of $MoS_2$ linked with BDT were consistently red-shifted both for the pristine films ($MoS_2$-BDT-$MoS_2$) and the heterostructures ($MoS_2$-BDS-$WS_2$) for all delay times (**Figure 4c** and **Figure S19**). To investigate this in more detail, we compared the TA spectra of pristine and BDT-linked TMDs at different pump-probe delay times (**Figure S20**). At late delay times (i.e., 100-300 ps), after the TMD bandgaps returned to their ground state values, the spectral peaks should match the ground state differential transmission spectra. For both neat $MoS_2$ (**Figure S20b**) and the $MoS_2$-$WS_2$ heterostructure (**Figure S20f**), the TA spectra at 100-300 ps were red-shifted in the presence of BDT compared to the pristine TMDs. Red-shifts of the excitonic peaks of $MoS_2$ have been attributed to reduction in the exciton binding energy [R],[8] which suggests that the BDT molecule enables easier separation of the exciton compared to the unlinked heterostructure. We do not observe such red-shifts in $X_A$ of neat $WS_2$ in the presence of BDT at almost any delay time (**Figure S20c,d** and **Figure S19a**), suggesting that the BDT does not have as large of an effect on the exciton binding energy of $WS_2$ alone.

This is in stark contrast to the $X_A$ of $WS_2$ in the heterostructure, which exhibits completely different spectral shifts depending on either the formation of an interlayer exciton ($MoS_2$-$WS_2$) or charge separation ($MoS_2$-BDT-$WS_2$), as discussed in the main text (**Figure 4d**).

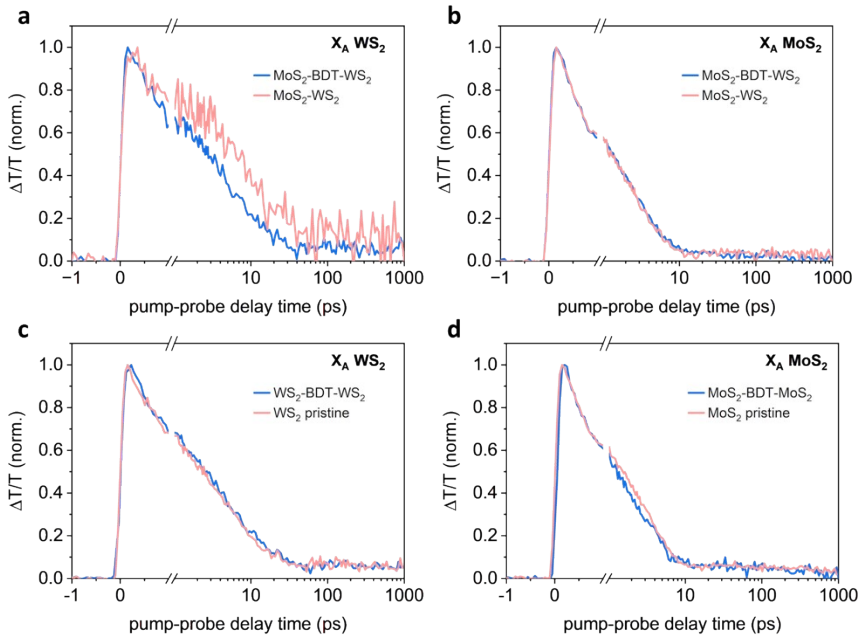


**Figure S21**. Transient absorption kinetic traces of the $X_A$ of $WS_2$ (a, c) and the $X_A$ of $MoS_2$ (b, d) within either the $MoS_2$-$WS_2$ heterostructures (a, b) or the isolated monolayers ($WS_2$ or $MoS_2$; c, d, respectively) with or without BDT.

The BDT-linked heterostructures exhibited faster relaxation dynamics compared to the unlinked heterostructures (**Figure S21**). $X_A$ of $WS_2$ in the unlinked $MoS_2$-$WS_2$ heterostructure had a much longer lifetime (7.7 ps) compared to the BDT-linked heterostructure (4.5 ps; **Figure S21a** and **Table S2**). This longer lifetime further supports formation of tightly bound interlayer excitons within the unlinked heterostructures, as described in the main text.[9] The interlayer excitons were not likely present for the BDT-linked heterostructures such that charge separation could thus proceed at a much faster rate. We note that this effect was most pronounced for the $X_A$ $WS_2$ excitons; $X_A$ of $MoS_2$ had nearly identical lifetimes with or without BDT (~2 ps; **Figure S21b** and **Table S2**). We further note that the lifetime of the $X_A$ $WS_2$ and $X_A$ $MoS_2$ excitons were unchanged in the isolated monolayer films with or without BDT (**Figure S21c, d** and **Table S2**). The long-lived species present in all samples at time scales >30 ps comes from trapped excitons,[10] which was significantly higher for the unlinked heterostructure (up to 11.8% for $X_A$ $WS_2$) compared with the BDT-linked one (up to 5.7% for $X_A$ $WS_2$) (**Table S2**), further demonstrating the reduction of sulfur vacancies upon BDT functionalization.

| Sample | Species | $A_0$ (%) | $A_1$ (%) | $t_1$ (ps) | $A_2$ (%) | $t_2$ (ps) | $t_{ave}$ (ps) |
|---|---|---|---|---|---|---|---|
| $MoS_2$ | $X_A$ ($MoS_2$) | 4.40 | 30.22 | 0.490 | 65.38 | 2.99 | 2.10 |
| $MoS_2$-BDT-$MoS_2$ | $X_A$ ($MoS_2$) | 4.10 | 53.79 | 0.968 | 42.10 | 3.67 | 2.06 |
| $MoS_2$-$WS_2$ | $X_A$ ($MoS_2$) | 3.06 | 36.14 | 0.626 | 60.79 | 2.82 | 1.94 |
| $MoS_2$-BDT-$WS_2$ | $X_A$ ($MoS_2$) | 2.09 | 41.64 | 0.618 | 56.26 | 3.30 | 2.11 |
| $WS_2$ | $X_A$ ($WS_2$) | 5.97 | 41.00 | 0.805 | 53.03 | 7.08 | 4.09 |
| $WS_2$-BDT-$WS_2$ | $X_A$ ($WS_2$) | 5.65 | 42.25 | 0.846 | 52.10 | 8.00 | 4.53 |
| $MoS_2$-$WS_2$ | $X_A$ ($WS_2$) | 11.78 | 21.57 | 0.532 | 66.65 | 11.35 | 7.68 |
| $MoS_2$-BDT-$WS_2$ | $X_A$ ($WS_2$) | 5.74 | 36.44 | 0.678 | 57.81 | 7.34 | 4.49 |

**Table S2.** Summary of fits of kinetic traces.

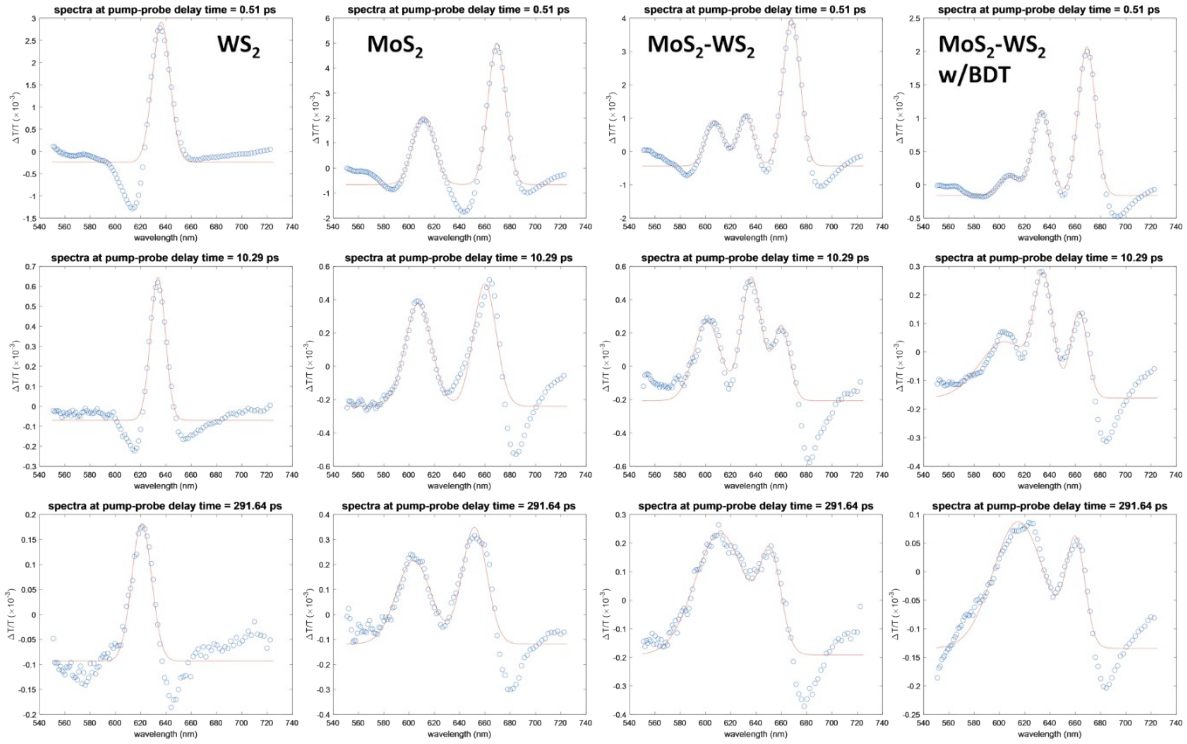


**Figure S22.** Examples of multi-Gaussian fits for the TA spectra at different pump-probe delay times. 1 Gaussian was used for $WS_2$; 2 Gaussians for $MoS_2$; and 3 Gaussians were initially used for the $MoS_2$-$WS_2$ heterostructures, with or without BDT. For the heterostructures, as one peak decayed, the peaks at later time scales were fit with only 2 Gaussians.

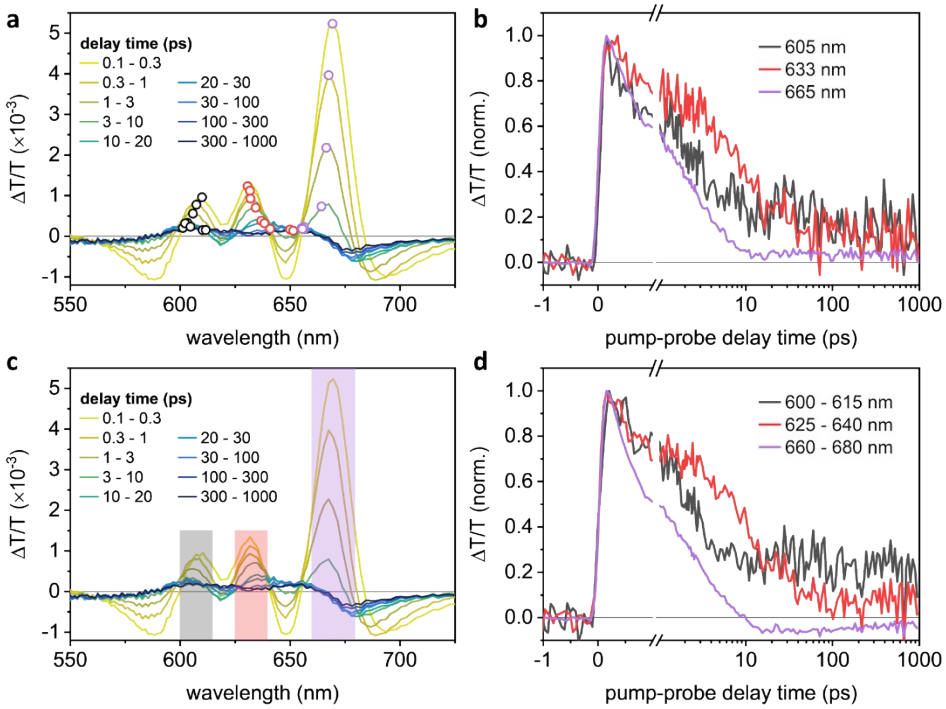


**Figure S23**. Example of tracing the kinetics of spectrally-shifting peaks (a,b) compared to tracing the kinetics by averaging over a fixed wavelength range (c,d). (a) TA spectra at different pump-probe delay times for pristine $MoS_2$-$WS_2$ heterostructure. Overlaid are the spectrally-shifting peak positions as determined from the multi-Gaussian fits. (b) Kinetic traces of the spectrally-shifting peaks as shown in (a) for each of the 3 dominant species: $X_A$ of $MoS_2$ (~665 nm); $X_A$ of $WS_2$ (~633 nm); and $X_B$ of $MoS_2$ (~605 nm). (c) Same TA spectra from (a), but the overlay shows the fixed wavelength range where the kinetics were spectrally averaged. (d) Kinetic traces of the fixed wavelength ranges shown in (c). Note the $X_A$ of $MoS_2$ signal drops to a negative value when the spectral shift is not taken into consideration.

## 8. Electrical characteristics in FET based on $MoS_2$-$WS_2$ heterostructure

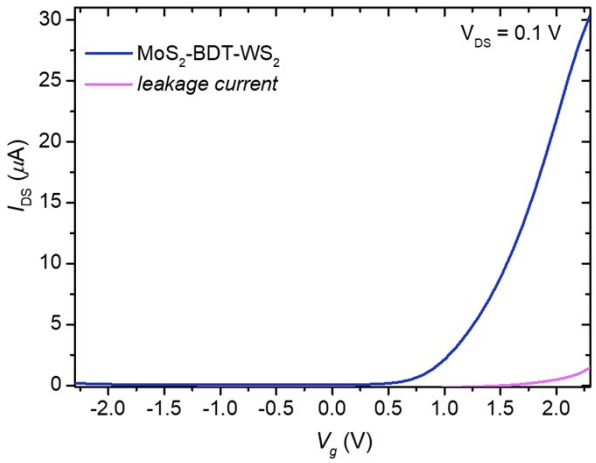


**Figure S24.** Leakage current in the champion device.

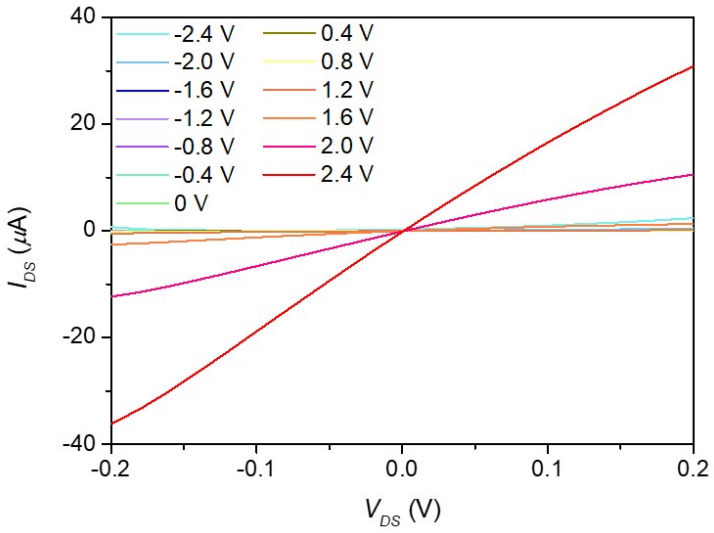


**Figure S25.** Output characteristics of an FET based on BDT-linked $MoS_2$-$WS_2$ heterostructure. Rectification behavior, typical of single $MoS_2$-$WS_2$ junction, cannot be observed in our BDT-linked $MoS_2$-$WS_2$ hetero-network because the drain current is averaged throughout the entire $MoS_2$-BDT-$WS_2$ channel network, as drain-source current must pass through multiple alternating $WS_2$-$MoS_2$ and $MoS_2$-$WS_2$ heterojunctions before reaching the source electrode. Also, it worth noting that both source and drain electrodes are in contact with different $MoS_2$ and $WS_2$ nanosheets simultaneously.

## 9. Field-effect mobility comparison

| Film | $\mu_{FE}$ (cm$^{-2}$ V$^{-1}$ s$^{-1}$) | $I_{ON}/I_{OFF}$ | $V_{th}$ (V) | SS (V dec$^{-1}$) |
|---|---|---|---|---|
| $MoS_2$-BDT-$MoS_2$ | (2.1 ± 0.2) x $10^{-2}$ | (1.0 ± 0.1) x $10^2$ | 1.2 ± 0.2 | 0.63 ± 0.09 |
| $WS_2$-BDT-$WS_2$ | (7.6 ± 0.1) x $10^{-2}$ | (2.6 ± 1.3) x $10^2$ | 1.7 ± 0.1 | 0.56 ± 0.02 |
| $MoS_2$-BDT-$WS_2$ | (1.6 ± 0.4) x $10^{-1}$ | (5.7 ± 2.0) x $10^2$ | 1.5 ± 0.2 | 0.31± 0.16 |

$\mu_{FE}$ = field-effect mobility; $I_{ON}/I_{OFF}$ = *ON:OFF ratio*; $V_{th}$ = *threshold voltage; SS = subthreshold swing*

**Table S3.** Mean values and standard deviation of key parameters calculated from the FETs based on BDT networks with $MoS_2$, $WS_2$ and $MoS_2/WS_2$ building units. Measurements have been carried out by sweeping $V_g$ between -2.3 and +2.3 V, with $V_{DS}$ = 0.1 V.

Charge carrier mobility of the FETs was calculated using the following equation[1]:

$$\mu = \frac{L}{C_v V_{DS} W t} \frac{\partial I_{DS}}{\partial V_G} \quad (4)$$

where $L_{ch}$ and $W_{ch}$ are the channel length and width (10 $\mu$m each), respectively, $V_{DS}$ is the source-drain voltage, $t$ is the film thickness, $C_v$ is the volumetric capacitance and $dI_{ds}/dV_g$ is the maximum slope extracted from the linear region of the transfer curves. $C_v$ values have been measured in our previous work,[1] which have been obtained by cyclic voltammetry in a three-electrode cell set-up with a Ag/AgCl reference electrode and a Pt counter electrode.

| Film | Deposition | Thickness | $\mu_{FE}$ (cm$^{-2}$ V$^{-1}$ s$^{-1}$) | Reference |
|---|---|---|---|---|

| | | (nm) | | |
|---|---|---|---|---|
| $MoS_2$-BDT-$WS_2$ network$^{(n)}$ | microfluidic | 45 ± 15 | 2.1 (1.6 ± 0.4) x $10^{-1}$ | *This work* |
| $MoS_2^{(n)}$ | spray coating | 500 ± 50 | (1.4 ± 0.6) x $10^{-3}$ | *Adv. Mater.* **2023**, *35*, 221115 |
| $MoS_2$-BDT network$^{(n)}$ | spray coating | 500 ± 50 | (1.2 ± 0.7) x $10^{-2}$ | *Adv. Mater.* **2023**, *35*, 221115 |
| $MoS_2^{(n)}$ | ink-jet printing | 20 | (6 ± 2) x $10^{-2}$ | *Adv. Electron. Mater.* **2021**, *7*, 2100112 |
| $MoS_2^{(n)}$ | drop casting | 700 ± 100 | $10^{-3}$ | *Nat. Nanotechnol.* **2021**, *16*, 592 |
| $WS_2^{(n)}$ | drop casting | 700 ± 100 | $10^{-3}$ | *Nat. Nanotechnol.* **2021**, *16*, 592 |
| $ReS_2^{(n)}$ | drop casting | 700 ± 100 | $10^{-4}$ | *Nat. Nanotechnol.* **2021**, *16*, 592 |
| $MoS_2$-BDT network$^{(n)}$ | drop casting | 700 ± 100 | $10^{-2}$ | *Nat. Nanotechnol.* **2021**, *16*, 592 |
| $WS_2$-BDT network$^{(n)}$ | drop casting | 700 ± 100 | $10^{-2}$ | *Nat. Nanotechnol.* **2021**, *16*, 592 |
| $ReS_2$-BDT network$^{(n)}$ | drop casting | 700 ± 100 | $10^{-3}$ | *Nat. Nanotechnol.* **2021**, *16*, 592 |
| $WS_2^{(n)}$ | spray coating | 150 ± 20 | 1.3 x $10^{-2}$ | *Adv. Funct. Mater.* **2018**, *29*, 1804387 |
| $MoS_2^{(n)}$ | spray coating | 2600 | 1.5 x $10^{-1}$ | *Science* **2017**, *356*, 69 |
| $WS_2^{(p)}$ | spray coating | 1800 | 2.2 x $10^{-1}$ | *Science* **2017**, *356*, 69 |

$^{(n)}$ = *n*-type; $^{(p)}$ = *p*-type

**Table S4.** Summary of $\mu_{FE}$ values based on various solution-processed 2D TMDs films. Mean values and standard deviation of $\mu_{FE}$ are in brackets, where available. It worth noting that TMDs films in cited works require thicknesses of hundreds/thousand nm to achieve sufficient percolation of charges.

References

1 A. G. Kelly, T. Hallam, C. Backes, A. Harvey, A. S. Esmaeily, I. Godwin, J. Coelho, V. Nicolosi, J. Lauth, A. Kulkarni, S. Kinge, L. D. A. Siebbeles, G. S. Duesberg and J. N. Coleman, *Science*, 2017, **356**, 69–73.
2 A. Syari'ati, S. Kumar, A. Zahid, A. A. E. Yumin, J. Ye and P. Rudolf, *Chem. Commun.*, 2019, **55**, 10384–10387.
3 C. Kastl, R. J. Koch, C. T. Chen, J. Eichhorn, S. Ulstrup, A. Bostwick, C. Jozwiak, T. R. Kuykendall, N. J. Borys, F. M. Toma, S. Aloni, A. Weber-Bargioni, E. Rotenberg and A. M. Schwartzberg, *ACS Nano*, 2019, **13**, 1284–1291.
4 B. Chakraborty, A. Bera, D. V. S. Muthu, S. Bhowmick, U. V. Waghmare and A. K. Sood, *Phys. Rev. B*, 2012, **85**, 161403.
5 E. P. Randviir and C. E. Banks, *Anal. Methods*, 2013, **5**, 1098–1115.
6 S. Wang, J. Zhang, O. Gharbi, V. Vivier, M. Gao and M. E. Orazem, *Nat. Rev. Methods Primers*, 2021, **1**, 1–21.
7 V. Montes-García, R. F. de Oliveira, Y. Wang, A. Berezin, P. Fanjul-Bolado, M. B. G. García, T. M. Hermans, D. Bonifazi, S. Casalini and P. Samorì, *Adv. Funct. Mater.*, 2021, **31**, 2008554.
8 M. Drüppel, T. Deilmann, P. Krüger and M. Rohlfing, *Nat. Commun.*, 2017, **8**, 2117.
9 P. Rivera, J. R. Schaibley, A. M. Jones, J. S. Ross, S. Wu, G. Aivazian, P. Klement, K. Seyler, G. Clark, N. J. Ghimire, J. Yan, D. G. Mandrus, W. Yao and X. Xu, *Nat. Commun.*, 2015, **6**, 6242.
10 A. Mondal, R. K. Yadav, M. Shrivastava, C. S. Rout, D. Karmakar and K. V. Adarsh, *Appl. Phys. Lett.*, 2020, **117**, 142104.